ACS OMEGA

Article

Cite This: ACS Omega 2019, 4, 19018−19029

http://pubs.acs.org/journal/acsodf

Ultrafast Detection of Low Acetone Concentration Displayed by Au-Loaded $LaFeO_3$ Nanobelts owing to Synergetic Effects of Porous 1D Morphology and Catalytic Activity of Au Nanoparticles

Katekani Shingange,[†,‡] Hendrik Swart,[‡] and Gugu H. Mhlongo*[,†,‡]

[†]DST/CSIR National Centre for Nanostructured Materials, Council for Scientific and Industrial Research, Pretoria 0001, South Africa

[‡]Department of Physics, University of Free State, Bloemfontein 9300, South Africa

ABSTRACT: Herein, we report on one-dimensional porous Au-modified $LaFeO_3$ nanobelts (NBs) with high surface area, which were synthesized through the electrospinning method. The incorporation and coverage of Au nanoparticles (NPs) on the surface of the $LaFeO_3$ NBs was achieved by adjusting the HAuCl amount in the precursor solution. Successful incorporation of Au NPs was examined by X-ray diffraction, high-resolution transmission electron microscopy, and X-ray photoelectron spectroscopy. The gas-sensing performance of both the pure and Au/$LaFeO_3$ NB-based sensors was tested toward 2.5−40 ppm of acetone at working temperatures in the range from room temperature to 180 °C. The gas-sensing findings revealed that Au/$LaFeO_3$ NB-based sensor with the Au concentration of 0.3 wt % displayed improved response of 125−40 ppm of acetone and rapid response and recovery times of 26 and 20 s, respectively, at an optimal working temperature of 100 °C. Furthermore, all sensors demonstrated an excellent response toward acetone and remarkable selectivity against NO_2, NH_3, CH_4, and CO. Hence, the Au/$LaFeO_3$-NB-based sensor is a promising candidate for sensitive, ultrafast, and selective acetone detections at low concentrations. The gas-sensing mechanism of the Au/$LaFeO_3$ sensors is explained in consideration of the catalytic activity of the Au NPs, which served as direct adsorption sites for oxygen and acetone.

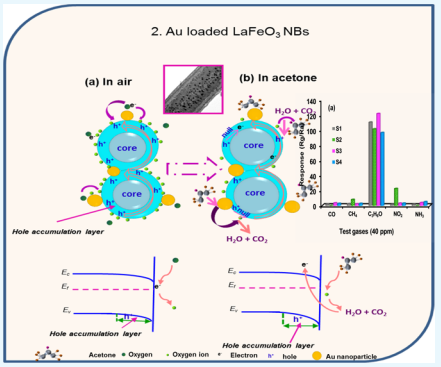

1. INTRODUCTION

In a quest for better living conditions through industrialization, comes the disadvantage of increase in air pollution by different types of toxic chemical compounds in air that can be harmful to human health. Acetone (C_3H_6O) is one of the potential volatile organic compounds with an aromatic smell used in medicine, coatings, and pesticides.[1−3] However, long exposure to certain concentrations of acetone may cause human health impact, such as eye, nose, and central nervous system damage.[4,5] Nonetheless, acetone has been classified as a useful component used as a breath biomarker for noninvasive diagnosis of type-1 diabetes.[6] It is reported that the average acetone concentration level for healthy human breath is 0.9 ppm, whereas for a diabetic patient, it's more than 1.8 ppm.[7] Therefore, it is essential to fabricate a sensor exhibiting high sensitivity, quick response/recovery time, and good stability at low concentrations of acetone.

Semiconductor metal oxides (SMO) have been regarded as a promising group of sensing materials because of their ease in fabrication, low cost, and sensitivity to a variety of reducing and oxidizing gases.[8−13] This group of sensing materials can be synthesized in a variety of dimensions ranging from 0 to 3 dimensions (0D−3D), with all different dimensions revealing different sensing properties.[14−16] Of all different dimensions of SMO, one-dimensional (1D) nanostructures, such as nanorods,[17] nanotubes,[18] nanofibers,[19] and nanobelts (NBs),[20,21] have been proven to give better gas-sensing performance since they possess large surface area and a strong adsorption/desorption ratio of the analyte gas molecules.[22−25] As one of the structures categorized under 1D family, nanobelts (NBs) are of particular interest as they display high surface area with interparticle contact, which are key parameters to facilitate the adsorption/desorption of gas molecules, thus contributing toward sensor performance enhancement.[26]

SMOs with n-type conductivity are mostly utilized as compared with the p-type counterparts since Hübner et al.[27] validated that the gas response obtained for a p-type material is a square root of the response of an n-type material having the same morphology. Nonetheless, p-type SMOs have distinctive catalytic activity with different volatile organic compounds,[28,29] thus making them potential candidates for the fabrication of innovative functionality in high-performance gas sensor devices. However, to successfully attain such innovation, it is of paramount importance to improve the gas response characteristics of these p-type SMOs to satisfy the demands for practical application, such as high sensitivity, selectivity, and fast response/recovery speed at low working temperatures to low concentration levels of analyte gas. For this reason, a

Received: July 1, 2019
Accepted: September 16, 2019
Published: November 5, 2019

DOI: 10.1021/acsomega.9b01989
ACS Omega 2019, 4, 19018−19029

number of strategies, ranging from construction of heterojunction composites,[30,31] control and variation of morphology,[32,33] UV light stimulation,[34,35] and noble metal functionalization,[36,37] have been adopted to overcome these hurdles. The aforementioned alterations can expose more surface area, thus increasing more active sites and effectively promote electron transfer, therefore resulting in improved gas-sensing performance.[38]

Incorporation of noble metals, such as Ag, Au, and Pd, has been proven to be more effective since noble metals bring about a chemical catalytic effect, whereby the noble metal acts as direct active sites for the adsorption of analyte gas and assists in the chemical reactions between the analyte gas and the sensing material.[1,18,39−43] Additionally, the noble metals can also fast-track the transfer of electrons to the surfaces of the sensing material.[38,44] These effects in gas sensing have been proven in many research works; for instance, Jin et al.[45] produced SnO_2 nanobelts functionalized with Au, which revealed decreased response and recovery times with higher response toward ethanol as compared with bare SnO_2. In another work by Majhi et al.,[46] it was found that Au@NiO core−shell nanoparticles revealed higher response than the pristine NiO nanoparticles to 100 ppm of ethanol at 200 °C.

Of all p-type SMOs that can be used in gas-sensing applications, $LaFeO_3$ has been identified as a promising gas sensor material due to its interesting properties, such high electrical conductivity and catalytic activity, for surface-driven redox reactions.[47−51] Moreover, its perovskite multimetal structure allows manipulation of its properties due to overlap between filled O^{2-} p-orbitals and the unfilled orbitals of the metal cations in relation to their monometal counterparts.[52] As much as $LaFeO_3$ is a well-known p-type SMO, only a few studies have been reported on the effects of noble metal catalysts (i.e., Ag) loading on its sensing abilities.[53,54] Moreover, reports on using Au as a catalyst for $LaFeO_3$ sensing are very scarce, especially for acetone sensing. Therefore, more investigations are needed to elucidate the Au-loading effects since Au is commended as a very good catalyst that can induce chemical sensitization, thus resulting in enhanced gas-sensing characteristics.[37,44,55,56]

In this context, this work focuses on the fabrication of Au-loaded $LaFeO_3$ NBs at different Au loading levels to investigate the effects that Au brings about on the gas-sensing performance of the $LaFeO_3$ NBs. Coupling the 1D NB morphology of $LaFeO_3$ with the catalytic activity of Au, the structural, morphological, and most crucially the gas-sensing performance will be thoroughly studied to establish the influence of Au loading. A possible gas-sensing mechanism will also be discussed to demonstrate the interaction taking place between the analyte gas and the sensor material surface.

2. EXPERIMENTAL SECTION

2.1. Materials Used. Lanthanum nitrate hexahydrate ($La(NO_3)_3{\cdot}6H_2O$), ferric nitrate nonahydrate ($Fe(NO_3)_3{\cdot}9H_2O$), gold(III) chloride solution ($HAuCl_4$), and poly(vinylpyrrolidone) (PVP) were used as the starting materials without further purification. The solvents used were *N*,*N*-dimethylformamide (DMF) and ethanol.

2.2. Preparation of the Electrospinning Precursor Solutions. Three solutions with different Au concentrations were prepared, and the procedure was as follows: 0.493 g of $Fe(NO_3)_3{\cdot}9H_2O$ and 0.521 g of $La(NO_3)_3{\cdot}6H_2O$ were dissolved in a mixed solution consisting of 7 mL of DMF and 3 mL of ethanol followed by stirring until completely dissolved. Appropriate amounts of HAuCl solution required to prepare 0.1, 0.3, and 0.5 wt % Au-loaded $LaFeO_3$ were then added into the mixture. Then, 1.5 g of PVP was added into the solution and continuously stirred to make the homogeneous gel precursor solution ready for electrospinning. For comparison purposes, the pure $LaFeO_3$ solution was prepared following the same procedure without the addition of the HAuCl solution.

2.3. Fabrication of the Pure and Au-Loaded $LaFeO_3$ NBs. For the electrospinning process, each of the prepared precursor solutions was transferred into a 10 mL glass syringe, with an inner diameter of 0.6 mm. A voltage of 20 kV was applied between the spinneret and the rotating drum collector with a spacing distance of 10 cm. The solution was continuously pumped by a syringe pump at a rate of 0.8 μL h^{-1}. The obtained NB composites were annealed at 550 °C for 2 h in air to obtain the Au-loaded $LaFeO_3$ NBs at a heating rate of 2 °C min^{-1}. For convenience, the unloaded sample was named S1 and Au-loaded $LaFeO_3$ samples were named S2, S3, and S4 for Au concentrations of 0.1, 0.3, and 0.5 wt %, respectively.

2.4. Characterization of the Pure and Au-Loaded $LaFeO_3$ NBs. The phase purity and crystallinity characteristics of S1−S4 were measured through X-ray diffraction (XRD) using a computer-controlled Panalytical X'pert PRO PW3040/60 X-ray diffractometer with Cu Kα (λ = 1.5405 Å) radiation. The morphology and elemental distribution analyses were performed using a ZEIS-AURIGA field-emission scanning electron microscope (SEM) and JEOL TEM-2100 transmission electron microscope (TEM) equipped with an electron-dispersive X-ray spectroscope (EDS). X-ray photoelectron spectroscopy (XPS) patterns were recorded on a PHI 5000 Versaprobe X-ray photoelectron spectroscope (XPS) equipped with monochromatic Al Kα radiation ($h\nu$ = 1486.6 eV). The specific surface areas and pore volumes of the samples were examined using a Micromeritics TRISTAR 3000 surface area analyzer.

2.5. Fabrication and Measurement of Gas Sensors Based on Pure and Au-Loaded $LaFeO_3$ NBs. The sensors based on S1, S2, S3, and S4 were prepared as follows: 40 mg of each sample was mixed with a solution of ethyl cellulose (a temporary binder) in turpineol and ground for a few minutes to make thixotropic pastes. The pastes were then coated onto an alumina substrate equipped with a pair of platinum (Pt) electrodes on the top surface and a heater at the bottom surface to control the operating temperature. The sensors were then heated at 300 °C for 2 h at a heating rate of 3 °C min^{-1} to achieve good adhesion. The gas-sensing performance was evaluated using a KSGAS6S gas-sensing station (KENOSIS-TEC, Italy). The atmospheric condition was controlled by means of MKS Instruments Deutschland GmbH mass flow controllers supplying desired concentrations of NH_3, C_3H_6O, NO_2, CO, and CH_4 into the sensing chamber by diluting the concentrated analyte gas in synthetic air. The operating temperature of the sensors was controlled by adjusting the heating voltage while using a thermocouple to measure the output temperature to correspond to temperatures from the room temperature (RT) to 180 °C. The changes in electrical resistance during the interaction of the analyte gas molecules and the surface of the $LaFeO_3$ NB-based sensors was measured in air (R_a) and in the presence of the analyte gas (R_g) by means of a Keithley 6487 Picoammeter/voltage source meter. Since

DOI: 10.1021/acsomega.9b01989
ACS Omega 2019, 4, 19018−19029

the NBs were annealed at 550 °C, the gas-sensing measurements were below 200 °C; so no thermally induced changes were expected in the sensing material. It is also important to mention that S1, S2, S3, and S4 are all p-type materials whose resistance increase in reducing gas- containing air and the sensor response can be determined by R_g/R_a.[50] The time taken by the sensor to reach 90% of the highest change in resistance after exposure to the analyte gas was measured as the response time while the time taken by the sensor to reach 90% of its original resistance was measured as the recovery time.

3. RESULTS AND DISCUSSION

3.1. Phase and Morphology Analysis. The phase purity and crystallinity of the obtained samples were determined using XRD, and the resulting diffraction patterns are shown in Figure 1. The X-ray diffraction patterns for S1 could be indexed to the $LaFeO_3$ perovskite phase with orthorhombic structure (JCPDS card no. 75-0541). Upon Au loading onto $LaFeO_3$ surface, a slight shift in diffraction peak positions of S2, S3, and S4 as compared with S1 was observed. Additional diffraction peaks located at 38.1, 44.3, 64.5, and 77.5° corresponding to (111), (200), (220), and (311) planes indexed to the cubic phase of Au (JCPDS card no. 04-0748) were also noted. Further, the decline in peak intensity upon Au incorporation suggests poor crystallinity of $LaFeO_3$ caused by the addition of Au. Moreover, peak broadening was observed with Au incorporation, indicating a decrease in crystallite size due to the addition of Au. Therefore, the mean crystallite sizes of S1, S2, S3, and S4 estimated from the Scherrer equation[55] using the (110) plane were found to be 20.7, 14.2, 15.3, and 25.6 nm, respectively. On the basis of these findings, it can be realized that the introduction of Au onto $LaFeO_3$ has an influence on the structural properties of $LaFeO_3$.

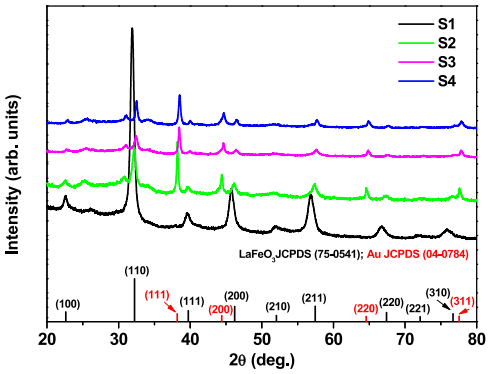

Figure 1. Diffraction patterns of S1, S2, S3, and S4, respectively.

Further, the morphological analysis of S1 to S4 was conducted through the use of SEM and the resulting micrographs of S1 to S4 are shown in Figure 2. Figure 2a presents the NBs before annealing, which revealed long nanobelts up to a few microns and around 3.2 μm in diameter. It was also noticed that the surface of the NBs was smooth and this is due to the presence of PVP, which acts as a template, thus assisting in maintaining the NB morphology.[57] It is worth mentioning that all as-spun NBs preserved this NB morphology regardless of the Au-loading level. Thus, only one image was used to represent the as-spun products. After

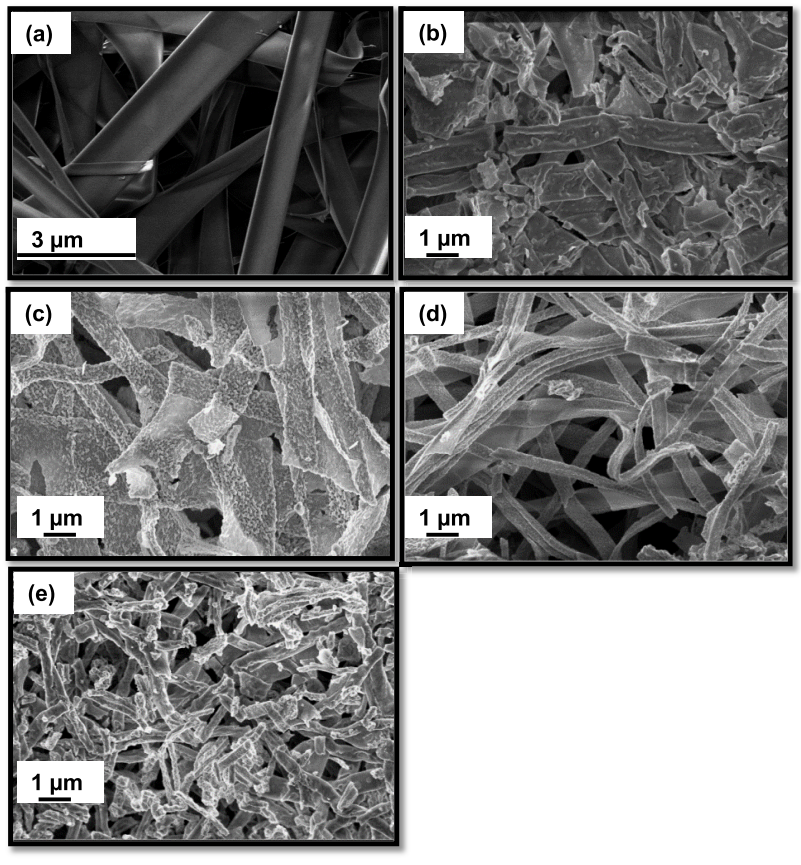

Figure 2. SEM images of the (a) as-spun, (b) S1, (c) S2, (d) S3, and (e) S4 NBs, respectively.

DOI: 10.1021/acsomega.9b01989
ACS Omega 2019, 4, 19018−19029

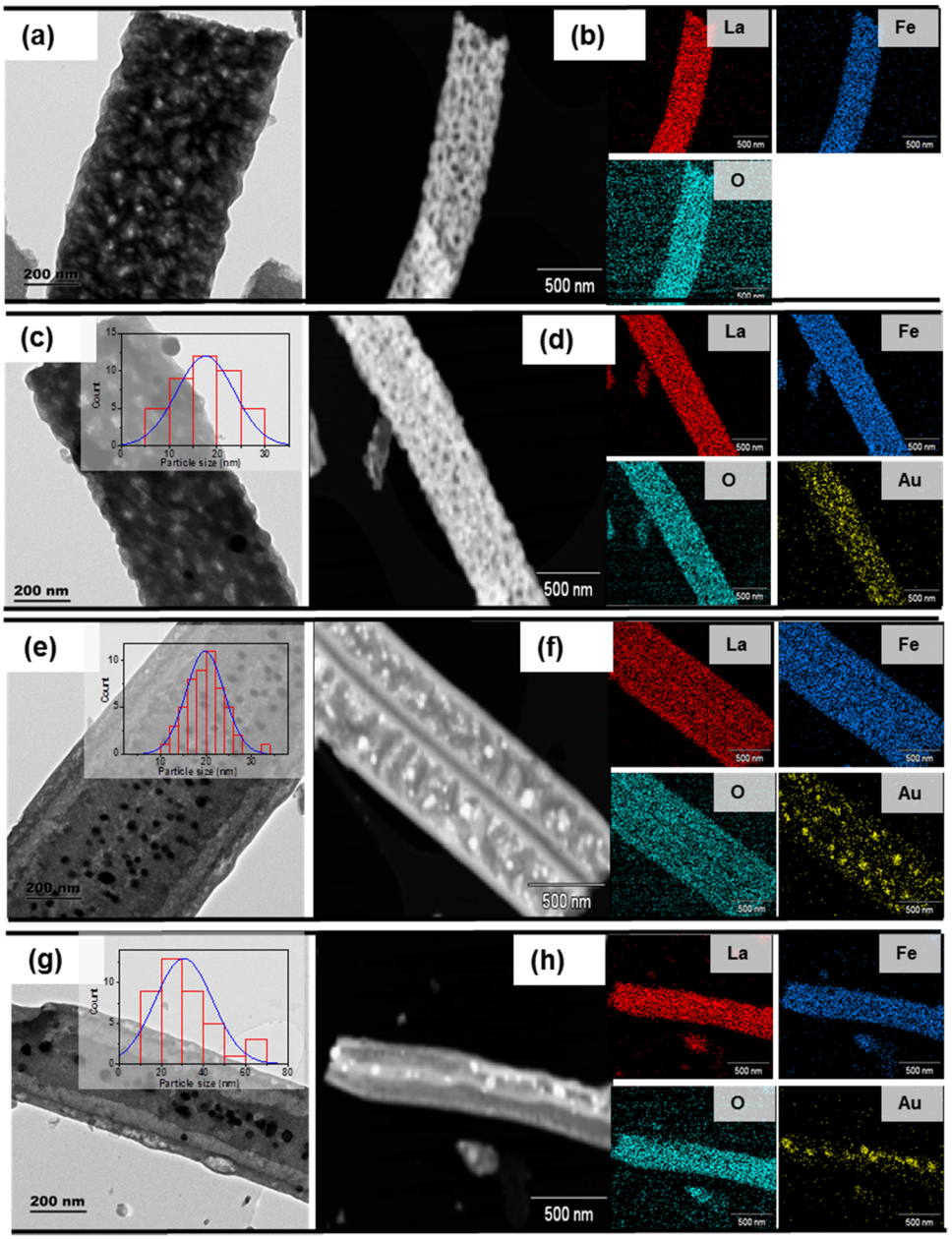

Figure 3. TEM images of (a) S1, (c) S2, (e) S3, and (g) S4 with their corresponding EDS maps (b, d, f, and h). Particle size distribution is represented as insets of each figure.

annealing, all obtained products (S1−S4) preserved the beltlike morphology; however, their average diameter was reduced to a range of 300 nm due to PVP decomposition during thermal annealing. Moreover, it was realized that the belts became very brittle as some of them were found to break since they contain a thinner section and also due to internal stress caused by the belt-structure shrinkage.[58,59]

Confirmation of the morphology was further done by high-resolution TEM (HRTEM), and the obtained images are presented in Figure 3. As observed in Figure 3a, the HRTEM micrograph for S1 revealed a beltlike structure composed of several single nanoparticles with an average grain size of ∼20 nm that were joined to each other to form a belt structure. As for S2, S3, and S4, a similar morphology to that of S1 was observed, except there were some very small particles belonging to Au distributed on the surface of each belt. The Au particle size distribution was estimated by measuring the diameter of the Au particles, and the plots are presented as insets of each TEM image per Au loading concentration. It was realized that the Au particle size grew from 17.5, 19.8, to 30.7 nm with increase in the Au loading level. Electron-dispersive spectroscopy (EDS) confirmed a uniform distribution of La, Fe, and O in the whole S1 belt, and Au was also detected for S2, S3, and S4. On the basis of these results, it is clear that Au has been successfully loaded onto the surface of the $LaFeO_3$ NBs.

3.2. Surface Area and Porosity Analysis. Generally, the sample's relative surface area and porosity are important parameters to determine gas-sensing performance as they can be favorable to provide active sites and gas diffusion pathways. Thus, the specific surface areas and the pore size of S1−S4 were determined by nitrogen adsorption−desorption measure-

DOI: 10.1021/acsomega.9b01989
ACS Omega 2019, 4, 19018−19029

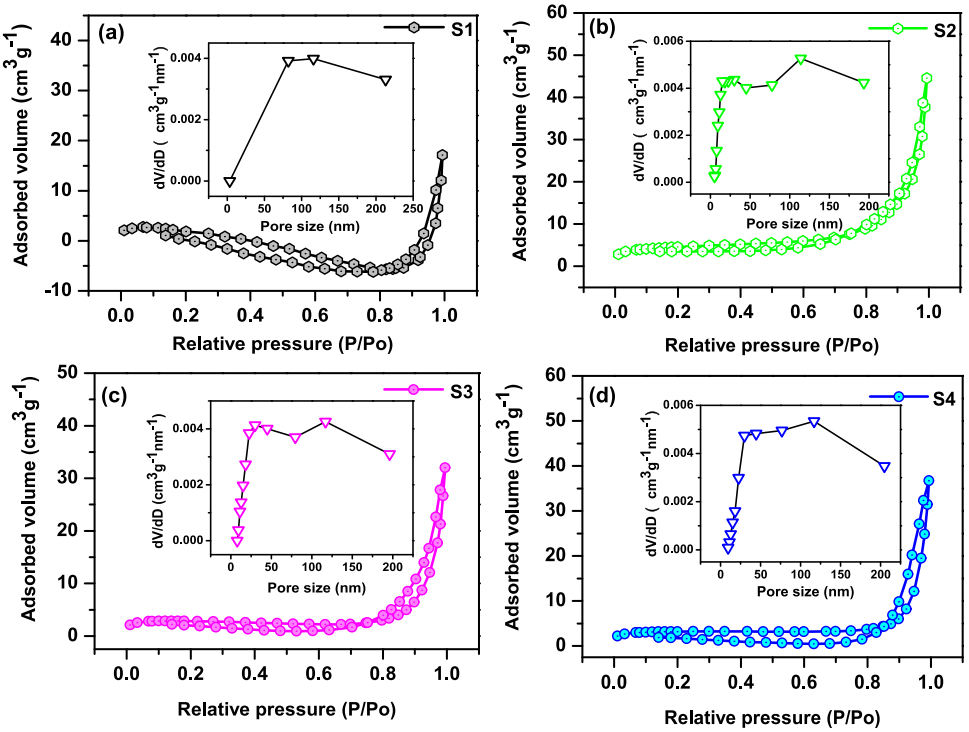

Figure 4. Nitrogen adsorption−desorption isotherms and the corresponding pore size distribution curves of (a) S1, (b) S2, (c) S3, and (d) S4.

ments. Figure 4 displays the nitrogen adsorption−desorption isotherms of S1, S2, S3, and S4. All isotherms exhibit a type IV isotherm, suggesting interconnected mesoporosity and high pore connectivity of the NBs.[39,60,61] According to the adsorption−desorption isotherms, the Brunauer−Emmett−Teller (BET) surface area values of S1, S2, S3, and S4 were found to be 5.8, 16.1, 9.1, and 10.9 $m^2\ g^{-1}$, respectively. The pore size distribution was determined using the Barrett−Joyner−Halenda (BJH) model analysis (see insets of Figure 4). The BJH pore size distribution indicated that S1, S2, S3, and S4 have an average pore diameter of 10.4, 29.4, 38.9, and 46.1 nm, respectively. The enhanced surface area and porosity can be attributed to the absence of clogging of the pores on the surface of $LaFeO_3$ as the Au nanoparticles are homogeneously distributed on the surface of each belt. Moreover, due to their very small size, the Au nanoparticles contribute to the overall surface area and porosity of the nanocomposites. The high surface area and porous structure is deemed beneficial in gas sensing as it can increase the sensing response and recovery speed by aiding the inward diffusion of the analyte gas or oxygen on the sensing material surface and the counter diffusion of reactant gases to the immediate ambient surroundings.[62]

3.3. Chemical Composition Analysis. The information regarding the electronic states and surface chemical composition of the samples was acquired through XPS measurements. In this case, the pure (i.e., S1) and highly Au-loaded (i.e., S4) samples were selected for this analysis. Figure 5 presents the recorded high-resolution spectra of La 3d, Fe 2p, Au 4f, and O 1s core levels of S1 and S4. As displayed in Figure 5a,b, the La 3d spectra acquired from both the S1 and S4 samples revealed two double peaks representing spin−orbit splitting components of La $3d_{5/2}$ and La $3d_{3/2}$ located at the 835.6 and 852.3 eV, respectively.[63] The split distance between the spin−orbit doublet was ∼16.7 eV, which is indicative of the La^{3+} state.[31,32,64] The La 3d spectrum from pure $La(OH)_3$, for example, will have four visible components, as in this case, even though there is only one chemical state.[65]

Similarly, the high-resolution spectrum of the Fe 2p core level from both the S1 and S4 presented in Figure 5c exhibited the spin−orbit splitting of the Fe $2p_{3/2}$ and Fe $2p_{1/2}$ core level states located at 709.9 and 723.5 eV with a spin−orbit splitting of 13.6 eV, which corresponds to the Fe^{3+} of $LaFeO_3$, respectively.[66,67] To gain more insight about the chemical state of Au loaded onto NB surface, the high-resolution spectrum of the Au 4f core level was recorded and is shown in Figure 5d. As shown in this figure, the Au 4f spectrum of the Au-loaded sample displayed a doublet at 85.1 and 88.6 eV for Au $4f_{7/2}$ and $4f_{5/2}$, respectively, which correspond to the A^0 state of metallic Au.[68] An additional peak belonging to Fe 3s was observed at a binding energy of 91.6 eV, confirming the interaction between Au and $LaFeO_3$. The high resolution of O 1s depicted in Figure 5e,f was Gaussian-fitted into three peaks corresponding to three types of oxygen states at the surface herein labeled as O_L at 528.9 and 530.4 eV, O_V at 531.2 and 531.5 eV, and O_C at 532.4 and 532.9 eV for S1 and S4, respectively. O_L can be assigned to O^{2-}, which is related to the bulk lattice oxygen, while O_V can be associated with surface-adsorbed oxygen (O^-) and is related to oxygen vacancies, and O_C corresponds to O_2^-, which is related to the chemisorbed species such as carbonates and hydroxyls, respectively.[69−71]

3.4. Gas-Sensing Performance of the Pure and Au-Loaded $LaFeO_3$ NBs. Normally, metal oxide-based gas sensors require heating to appropriate temperatures to achieve maximum response. The sensor response is usually defined as R_a/R_g for reducing gases and as R_g/R_a for oxidizing gases, where R_a is the sensor resistance in air and R_g is the sensor resistance in the presence of the target gas.[72] So to determine the operating temperature for S1−S4-based sensors, acetone responses at a concentration of 40 ppm at RT (23 °C), 100,

DOI: 10.1021/acsomega.9b01989
ACS Omega 2019, 4, 19018−19029

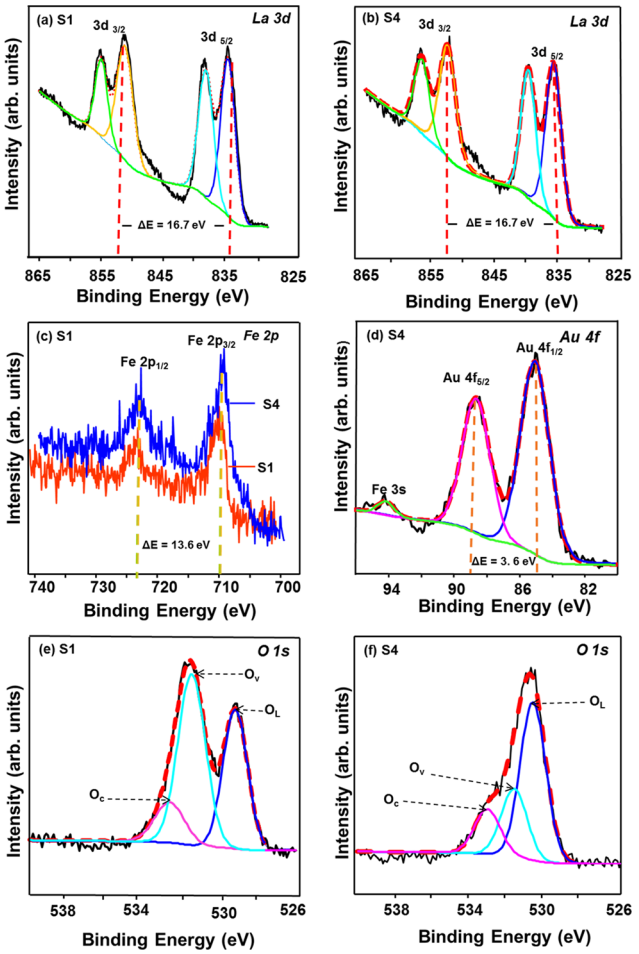

Figure 5. (a) High-magnification XPS spectra of (a, b) La 3d for S1 and S4, (c) Fe 2p for S1 and S4, (d) Au 4f for S4, (e, f) O 1s core levels of the for S1 and S4.

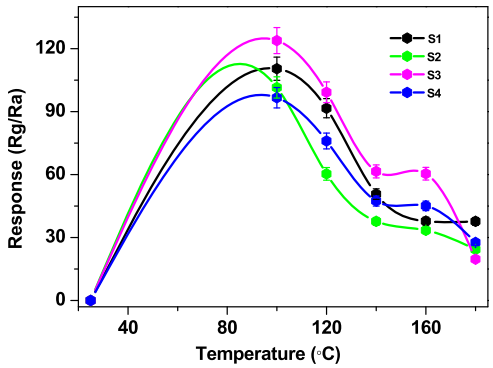

Figure 6. Responses of the S1-, S2-, S3-, and S4-based sensors to 40 ppm acetone at different operating temperatures.

120, 140, 160, and 180 °C were measured and the results are illustrated in Figure 6. An obvious response dependence on the operating temperature can be observed. With an increase in the operating temperature, the responses of all sensors were shown to increase to a maximum at 100 °C, then decrease with further increase of temperature toward 140−180 °C. The low responses displayed by all sensors at low operating temperatures is a common behavior for SMO as the analyte gas molecules do not have enough thermal energy to interact with the adsorbed surface oxygen species, thus giving a low response. But gradual increase of the operating temperature provides the analyte gas molecules with enough thermal energy to get activated and react with the surface-adsorbed oxygen species, therefore giving a high response. However, with further increase to higher temperatures, the rate of analyte gas adsorption and the usage of the sensing layer become reduced, resulting in the weakening of the sensor response.[51,73] The response values were found to be 112, 102, 125, and 96 for the sensors based on S1, S2, S3, and S4. From the obtained values, it can be clearly seen that the Au loading levels have an impact on the response of the $LaFeO_3$ NBs. The loading concentration determines the distribution and size of Au nanoparticles on the surface of the $LaFeO_3$ NBs, which strongly affects the gas-sensing response owing to the electronic and chemical catalytic stimulation of the Au nanoparticles, which strongly depend on the Au nanoparticle size and distribution.[74] Thus, it is important to obtain a suitable amount of Au loading for effective improvement of acetone response by $LaFeO_3$ NB-based sensors. On the basis of the above temperature dependence studies and findings, all acetone measurements on S1, S2, S3, and S4 were carried out at 100 °C.

To gain more insight on the effect induced by the Au nanoparticles on the surface of the $LaFeO_3$ NBs; S1−S4-based sensors were subjected to 2.5−40 ppm of acetone as a function of time at an operating temperature of 100 °C and the resulting curves are shown in Figure 7. All sensors displayed an increase and decrease in sensor resistance upon exposure to acetone and in air, which is typical of p-type SMO upon exposure to a reducing gas.[75] Moreover, the increase and decrease in resistance upon contact and removal of the acetone gas demonstrates the reversible interaction between the sensing material and the analyte gas. This reversible interaction takes a specific time, i.e., response and recovery time, which is very important for the practical application of gas sensors for efficiency and reliability purposes. The response times of the of S1−S4-based sensors to 40 ppm acetone were determined as 100, 70, 26, and 35 s, whereas the recovery times were found to be 17, 22, 20, and 9 s for S1, S2, S3, and S4, respectively. Fast response and recovery times were obtained for S2, S3, and S4, which can be attributed to the better accessibility of active sites and ease in diffusion due to the porous structures, coupled with the Au nanoparticle catalytic effect. Generally, the response of a sensor is dependent on the concentration of the target gas, and this relation is clearly displayed in Figure 7e for the response to acetone in the range from 2.5 to 40 ppm. Even though the lowest concentration experimentally examined was 2.5 ppm, the theoretical limit of detection (signal-to-noise ratio > 3) was estimated from Figure 7e to be around 0.056, 0.382, 0.267, and 0.733 ppm for S1, S2, S3, and S4, respectively. The limit of detection of less than 1 ppm to acetone with high response validates the promising use of the Au-loaded $LaFeO_3$ NBs in high-performance sensors for acetone detection.

As much as a sensor can give high response and fast response kinetics, it is also very crucial for the sensor to be able to selectively detect the target gas in the midst of other gases since real application atmospheres consist of a mixture of gases. With that said, the ability to single out acetone in the presence of other gases, such as CO, CH_4, NO_2, and NH_3 of S1-, S2-, S3-, and S4-based sensors at 100 °C was measured by exposing the sensors to 40 ppm of each test gas. The obtained results are displayed in Figure 8. All sensors demonstrate outstanding

DOI: 10.1021/acsomega.9b01989
ACS Omega 2019, 4, 19018−19029

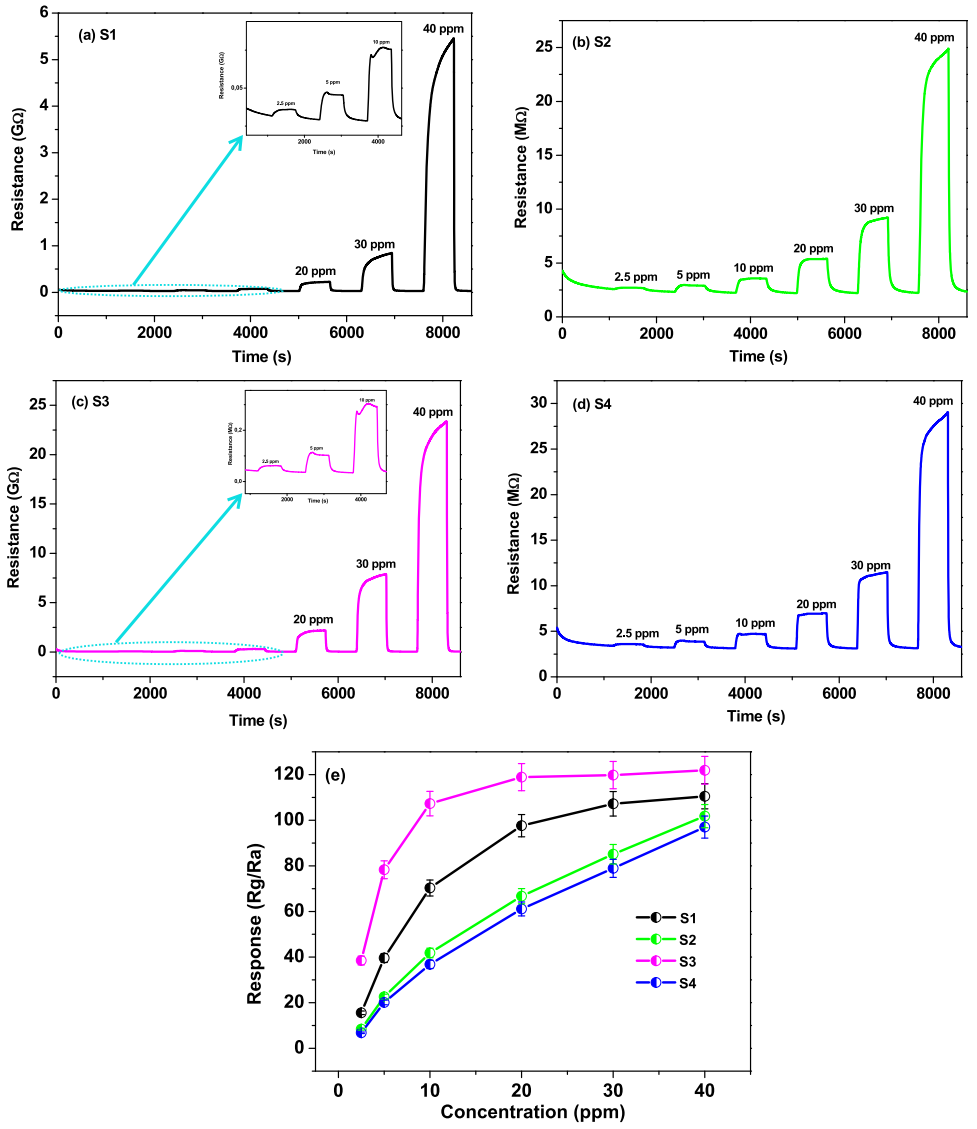

Figure 7. Dynamic resistance curves of (a) S1, (b) S2, (c) S3, and (d) S4 and (e) corresponding responses of S1−S4 to acetone concentrations ranging from 2.5 to 40 ppm.

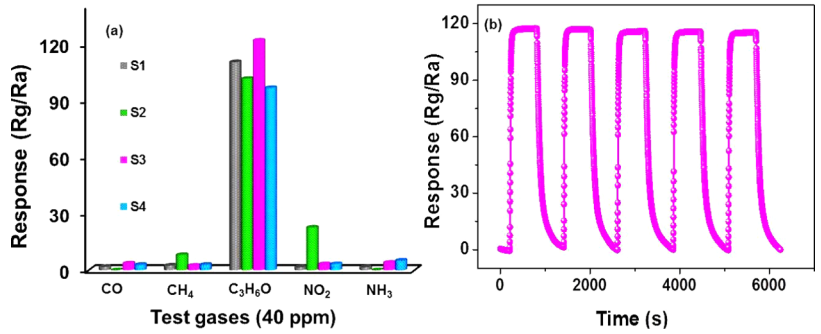

Figure 8. (a) Gas responses to 40 ppm of different gases and (b) reproducibility of S3 to 40 ppm acetone at 100 °C.

selectivity toward acetone molecules with S3 sensor displaying the highest response with minor responses toward interfering gases. The observed high selectivity toward acetone could probably be due to the fact that acetone is more chemically reactive with the adsorbed oxygen species at the optimum temperature (100 °C),[76,77] whereas the response to the other gas species is rather trivial probably due to the relative weak chemical interaction between them and the adsorbed oxygen species on the sensors' surface. Further, reproducibility of the sensor response is another important key factor in practical applications. Therefore, the reproducibility test to five response/recovery cycles of the sensor based on S3 was conducted and the results are shown in Figure 8b. The results demonstrated consistent high response with excellent recovery

DOI: 10.1021/acsomega.9b01989
ACS Omega 2019, 4, 19018−19029

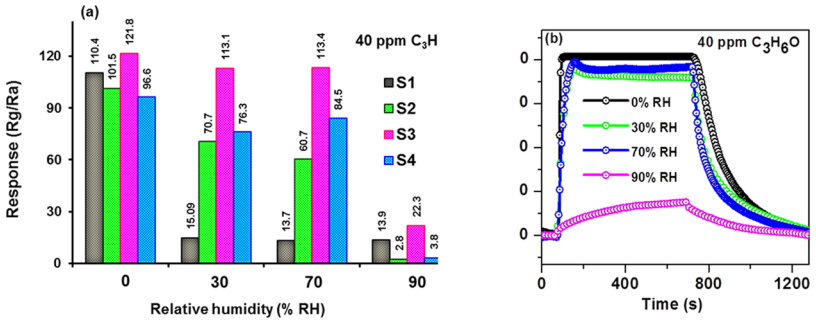

Figure 9. (a) Response histogram of S1−S4-based sensors and (b) S3 response and recovery curves to 40 ppm acetone in dry air and under different relative humidity of 30, 70, and 90% at 100 °C.

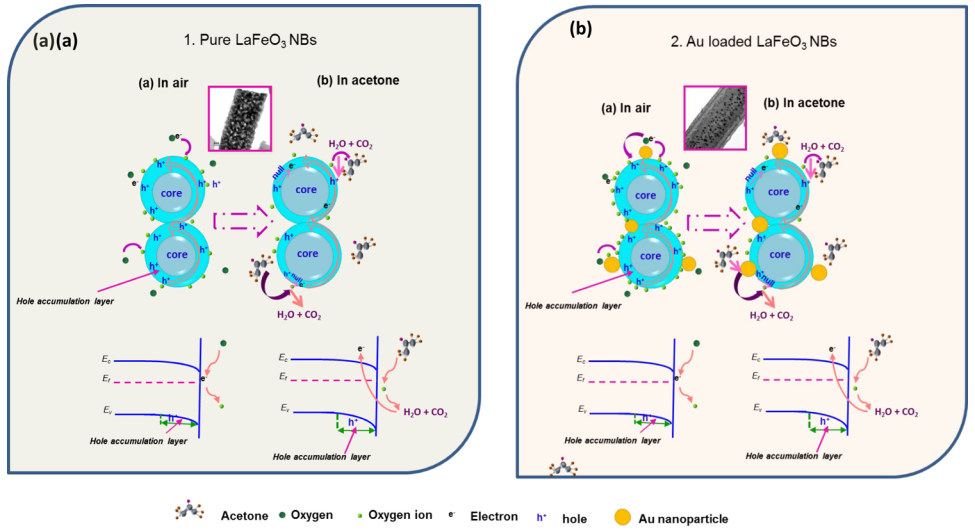

Figure 10. Proposed acetone sensing mechanism of the (a) pure and (b) Au-loaded $LaFeO_3$ NBs.

Table 1. Gas-Sensing Characteristics Based on $LaFeO_3$ Nanostructures Reported in the Recent Literature and This Work

sensing material	T (°C)	Conc. (ppm)	R_g/R_a	T_{res}/T_{rec} (s)	refs
Sr-doped $LaFeO_3$	275	500	0.70	20/270	84
2 wt % Pd-doped $LaFeO_3$	200	1	1.9	4/2	85
MIT Ag−$LaFeO_3$ spheres	155	5	23.3	55/60	81
$LaFeO_3$ thick film	260	0.5	2.068	62/107	86
$La_{0.68}Pb_{0.32}FeO_3$	200	50	7	60/20	87
$LaFeO_3$	400	80	204	15	88
porous $LaFeO_3$	240	200	12.2	9/18	89
0.3 wt % Au-loaded $LaFeO_3$	100	40	125	26/20	this work

without any obvious degradation of the sensor response, indicating good stability and reproducibility.

Usually, acetone is accompanied by moisture; therefore, it is important to take into consideration the effect of moisture on the sensing performance for practical applications. Thus, the comparison of the responses of S1−S4-based sensors toward 40 ppm of acetone both in dry and relative humidity (RH) conditions of 30, 70, and 90% at 100 °C were recorded and are represented by the histogram in Figure 9a. An obvious decline in response to acetone for both the pure and Au-loaded $LaFeO_3$ was observed with relative humidity increment from 30 to 90%. The decline of response with increasing relative humidity is a result of the competition between the hydroxyl species and the acetone molecules during the surface reactions, which lowers the oxygen adsorption, therefore reducing the sensor response.[78,79] Interestingly, S3-based sensor still revealed the highest response in all RH levels whereby it showed a small drop in response at 30−70% RH and a significant decrease in its response was observed at a higher relative humidity of 90% (see Figure 9b). The good sensing response of S3 even in a wide range of relative humidity conditions validates the practical applicability of the sensor.

3.5. Acetone Sensing Mechanism. In general, for SMO gas sensors, the most widely accepted sensing mechanism relies on the type of material's majority charge carriers (electrons or holes), its surface groups (i.e., O^{2-}, O^-, O_2^-), and the nature of the surface (acidic or basic surface), which mainly determine the adsorption−desorption interaction between the analyte gas and the sensing material. $LaFeO_3$ is regarded as a p-type SMO with the holes being the majority charge carriers while its gas-sensing mechanism is based on the changes of resistance in air and in the presence of the analyte gas.

When considering the pure $LaFeO_3$ NBs in air (Figure 9(1a)), neutral oxygen molecules adsorb on the $LaFeO_3$ surface and get partially ionized into O^{2-}, O^-, or O_2^- ions by attracting electrons from the valence band at different temperatures. Since the sensors in this work were operated at 100 °C, O^{2-} ions are more dominant than any other oxygen adsorbate.[80] Exposure of the $LaFeO_3$ sensors to the ambient

DOI: 10.1021/acsomega.9b01989
ACS Omega 2019, 4, 19018−19029

atmosphere then led to the formation of a thick underlying hole accumulation layer, which allowed the sensor to have a relatively low resistance layer covering the whole surface of the sensor. On the other hand, when the $LaFeO_3$-based sensors came into contact with acetone molecules (see Figure 10(1b)), a reaction between the acetone molecules and the oxygen adsorbates took place to form CO_2 and H_2O according to the following relation[81]

$$CH_3COCH_3 + 8O^{2-}_{(ads)} \rightarrow 3CO_2 + 3H_2O + 8e^- \quad (1)$$

This reaction then led to the release of electrons to the valence band, resulting in the recombination of electrons and holes.[81] As a result, the concentration of the holes was decreased and this led to an increase in the resistance of the $LaFeO_3$-based sensor. In the case of S3 (0.3 wt % Au-loaded $LaFeO_3$) in Figure 10 (2(a,b)), the acetone sensing mechanism follows the same process as that on the pure $LaFeO_3$; however, the electronic and chemical sensitization of the Au nanoparticles promotes enhancement in the sensing performance of the $LaFeO_3$ NB-based sensor.[82] The significant enhancement in the sensing performance of S3 may be explained as follows:

(i) Au is a good catalyst for oxygen dissociation,[83] which means that Au nanoparticles aid in ease of oxygen molecule adsorption and the capture of electrons to produce active oxygen adsorbates (Figure 10(2a)). Further, acetone molecules are ionized to active radicals by the Au nanoparticles and due to the spill-over effect of Au, these active radicals spill over the surface of $LaFeO_3$, facilitating the sensing reactions on the surface of $LaFeO_3$, thus enhancing the response and also fast-tracking response and recovery times.

(ii) The surface area and pore diameter increased with Au loading, as confirmed from BET analysis, and this can provide more surface adsorption sites to adsorb oxygen and acetone molecules and also ease in diffusion, hence the improved gas-sensing response.

(iii) The 1D NB morphology of $LaFeO_3$ also plays an important role as it allows overlapping of the hole accumulation layers along the NB direction resulting in continuous hole transfer channels, thus contributing to enhancement of the sensor performance.

Through literature survey it was realized that there are some acetone sensors based on $LaFeO_3$ nanostructures, which display different sensing capabilities. Table 1 lists some of the literature sampled through systems that are close to the work reported herein for comparison purposes. In comparison with the literature, it can be realized that S3 displays high response to a low concentration of acetone (40 ppm) at a relatively low operating temperature with quick response and recovery speed, thus ensuring a low power consuming operation with fast response kinetics. Moreover, S3 revealed good repeatability to a few response−recovery cycles, indicating stability and reproducibility, which are critical characteristics for practical applications. Thus, the S3-based sensor possesses valuable gas-sensing characteristics that deem it fit for practical applications.

4. CONCLUSIONS

In summary, a series of 1D Au-loaded $LaFeO_3$ NBs have been successfully synthesized via the electrospinning technique. The size and distribution of the Au nanoparticles on the surface of the $LaFeO_3$ NBs was controlled by adjusting the dosage of HAuCl. When tested for gas-sensing performance, all Au-loaded $LaFeO_3$ NBs, including the pure $LaFeO_3$ exhibited good selectivity and high response to acetone at an operating temperature of 100 °C with the 0.3 wt % Au-loaded $LaFeO_3$ NB-based sensor displaying the highest response in comparison with the other sensors. The gas-sensing behavior displayed by this sensor is closely related to the size and distribution of the Au nanoparticles, which controls the catalytic activity of the Au catalyst. Moreover, the increased surface area and porosity induced by Au addition on the 1D NB structure also played an essential role in the increasing gas-sensing performance of the S3-based sensor. The Au-doped $LaFeO_3$ sensor with Au content of 0.3 wt % offers a new strategy to prepare noble metal-modified $LaFeO_3$ NBs that can be promisingly employed to produce excellent and reliable gas sensors to low target gas concentrations at low operating temperatures.

AUTHOR INFORMATION

Corresponding Author

*E-mail: GMhlongo@csir.co.za. Tel.: +27 12 841 3935.

ORCID

Hendrik Swart: 0000-0001-5233-0130

Gugu H. Mhlongo: 0000-0002-7888-1069

Notes

The authors declare no competing financial interest.

ACKNOWLEDGMENTS

This work was financially supported by the department of Science and Technology of South Africa and the Council for Scientific and Industrial Research (DST/CSIR), Project numbers CGER85X and C1FNSO1. We acknowledge the National Centre for Nanostructured Materials (NCNSM) characterization facility and the University of Free State for the XPS measurements, under the umbrella of the DST/NRF Sarchi chair in Advanced and Luminescent Materials (grant 84415).

REFERENCES

(1) Guo, L.; Chen, F.; Xie, N.; Kou, X.; Wang, C.; Sun, Y.; Liu, F.; Liang, X.; Gao, Y.; Yan, X.; et al. Ultra-sensitive sensing platform based on Pt-ZnO-In_2O_3 nanofibers for detection of acetone. *Sens. Actuators, B* **2018**, *272*, 185−194.

(2) Satoh, T.; Omae, K.; Nakashima, H.; Takebayashi, T.; Matsumura, H.; Kawai, T.; Nakaza, M.; Sakurai, H. Relationship between acetone exposure concentration and health effects in acetate fiber plant workers. *Int. Arch. Occup. Environ. Health* **1996**, *68*, 147−153.

(3) Yang, X.; Zhang, S.; Yu, Q.; Sun, P.; Liu, F.; Lu, H.; Yan, X.; Zhou, X.; Liang, X.; Gao, Y.; Lu, G. Solvothermal synthesis of porous $CuFe_2O_4$ nanospheres for high performance acetone sensor. *Sens. Actuators, B* **2018**, *270*, 538−544.

(4) Jia, Q.; Ji, H.; Zhang, Y.; Chen, Y.; Sun, X.; Jin, Z. Rapid and selective detection of acetone using hierarchical ZnO gas sensor for hazardous odor markers application. *J. Hazard. Mater.* **2014**, *276*, 262−270.

(5) Wang, L.; Teleki, A.; Pratsinis, S. E.; Gouma, P. Ferroelectric WO_3 nanoparticles for acetone selective detection. *Chem. Mater.* **2008**, *20*, 4794−4796.

(6) Sun, X.; Ji, H.; Li, X.; Cai, S.; Zheng, C. Mesoporous In_2O_3 with enhanced acetone gas-sensing property. *Mater. Lett.* **2014**, *120*, 287−291.

(7) Rydosz, A. Sensors for Enhanced Detection of Acetone as a Potential Tool for Noninvasive Diabetes Monitoring. *Sensors* **2018**, *18*, 2298.

DOI: 10.1021/acsomega.9b01989
ACS Omega 2019, 4, 19018−19029

(8) Kolmakov, A.; Moskovits, M. Chemical sensing and catalysis by one-dimensional metal-oxide nanostructures. *Annu. Rev. Mater. Res.* **2004**, *34*, 151−180.
(9) Barsan, N.; Weimar, U. Conduction model of metal oxide gas sensors. *J. Electroceram.* **2001**, *7*, 143−167.
(10) Arafat, M.; Haseeb, A.; Akbar, S. A selective ultrahigh responding high temperature ethanol sensor using TiO_2 nanoparticles. *Sensors* **2014**, *14*, 13613−13627.
(11) Fan, F.; Feng, Y.; Tang, P.; Chen, A.; Luo, R.; Li, D. Synthesis and gas sensing performance of dandelion-like ZnO with hierarchical porous structure. *Ind. Eng. Chem. Res.* **2014**, *53*, 12737−12743.
(12) Mhlongo, G.; Motaung, D.; Kortidis, I.; Mathe, N.; Ntwaeaborwa, O.; Swart, H.; Mwakikunga, B.; Ray, S.; Kiriakidis, G. A study on the sensing of NO_2 and O_2 utilizing ZnO films grown by aerosol spray pyrolysis. *Mater. Chem. Phys.* **2015**, *162*, 628−639.
(13) Shingange, K.; Swart, H.; Mhlongo, G. H_2S detection capabilities with fibrous-like La-doped ZnO nanostructures: A comparative study on the combined effects of La-doping and post-annealing. *J. Alloys Compd.* **2019**, *797*, 284−301.
(14) Shingange, K.; Tshabalala, Z.; Dhonge, B.; Ntwaeaborwa, O.; Motaung, D.; Mhlongo, G. 0D to 3D ZnO nanostructures and their luminescence, magnetic and sensing properties: Influence of pH and annealing. *Mater. Res. Bull.* **2017**, *85*, 52−63.
(15) Ding, H.; Ma, J.; Yue, F.; Gao, P.; Jia, X. Size and morphology dependent gas-sensing selectivity towards acetone vapor based on controlled hematite nano/microstructure (0D to 3D). *J. Solid State Chem.* **2019**, *276*, 30−36.
(16) Mo, Y.; Shi, F.; Qin, S.; Tang, P.; Feng, Y.; Zhao, Y.; Li, D. Facile Fabrication of Mesoporous Hierarchical Co-doped ZnO for Highly Sensitive Ethanol Detection. *Ind. Eng. Chem. Res.* **2019**, *58*, 8061−8071.
(17) Shingange, K.; Mhlongo, G. H.; Motaung, D. E.; Ntwaeaborwa, O. M. Tailoring the sensing properties of microwave-assisted grown ZnO nanorods: Effect of irradiation time on luminescence and magnetic behaviour. *J. Alloys Compd.* **2016**, *657*, 917−926.
(18) Fu, J.; Zhao, C.; Zhang, J.; Peng, Y.; Xie, E. Enhanced Gas Sensing Performance of Electrospun Pt-Functionalized NiO Nanotubes with Chemical and Electronic Sensitization. *ACS Appl. Mater. Interfaces* **2013**, *5*, 7410−7416.
(19) Zhao, S.; Shen, Y.; Yan, X.; Zhou, P.; Yin, Y.; Lu, R.; Han, C.; Cui, B.; Wei, D. Complex-surfactant-assisted hydrothermal synthesis of one-dimensional ZnO nanorods for high-performance ethanol gas sensor. *Sens. Actuators, B* **2019**, *286*, 501−511.
(20) Qu, F.; Zhou, X.; Zhang, B.; Zhang, S.; Jiang, C.; Ruan, S.; Yang, M. Fe_2O_3 nanoparticles-decorated MoO_3 nanobelts for enhanced chemiresistive gas sensing. *J. Alloys Compd.* **2019**, *782*, 672−678.
(21) Li, J.; Liu, H.; Fu, H.; Xu, L.; Jin, H.; Zhang, X.; Wang, L.; Yu, K. Synthesis of 1D α-MoO_3/0D ZnO heterostructure nanobelts with enhanced gas sensing properties. *J. Alloys Compd.* **2019**, *788*, 248−256.
(22) Chen, J.; Xu, L.; Li, W.; Gou, X. α-Fe_2O_3 nanotubes in gas sensor and lithium-ion battery applications. *Adv. Mater.* **2005**, *17*, 582−586.
(23) Chen, Y.-J.; Meng, F.-n.; Yu, H.-l.; Zhu, C.-l.; Wang, T.-s.; Gao, P.; Ouyang, Q.-y. Sonochemical synthesis and ppb H_2S sensing performances of CuO nanobelts. *Sens. Actuators, B* **2013**, *176*, 15−21.
(24) Choi, Y.-J.; Hwang, I.-S.; Park, J.-G.; Choi, K. J.; Park, J.-H.; Lee, J.-H. Novel fabrication of an SnO_2 nanowire gas sensor with high sensitivity. *Nanotechnology* **2008**, *19*, No. 095508.
(25) Kruefu, V.; Wisitsoraat, A.; Tuantranont, A.; Phanichphant, S. Ultra-sensitive H_2S sensors based on hydrothermal/impregnation-made Ru-functionalized WO_3 nanorods. *Sens. Actuators, B* **2015**, *215*, 630−636.
(26) Kim, H.-J.; Lee, J.-H. Highly sensitive and selective gas sensors using p-type oxide semiconductors: Overview. *Sens. Actuators, B* **2014**, *192*, 607−627.
(27) Hübner, M.; Simion, C. E.; Tomescu-Stănoiu, A.; Pokhrel, S.; Bârsan, N.; Weimar, U. Influence of humidity on CO sensing with p-type CuO thick film gas sensors. *Sens. Actuators, B* **2011**, *153*, 347−353.
(28) Liu, H.; He, Y.; Nagashima, K.; Meng, G.; Dai, T.; Tong, B.; Deng, Z.; Wang, S.; Zhu, N.; Yanagida, T.; Fang, X. Discrimination of VOCs molecules via extracting concealed features from a temperature-modulated p-type NiO sensor. *Sens. Actuators, B* **2019**, 342.
(29) Park, H. J.; Hong, S. Y.; Chun, D. H.; Kang, S. W.; Park, J. C.; Lee, D.-S. A highly susceptive mesoporous hematite microcube architecture for sustainable P-type formaldehyde gas sensors. *Sens. Actuators, B* **2019**, *287*, 437−444.
(30) Na, C. W.; Woo, H.-S.; Kim, I.-D.; Lee, J.-H. Selective detection of NO_2 and C_2H_5OH using a Co_3O_4-decorated ZnO nanowire network sensor. *Chem. Commun.* **2011**, *47*, 5148−5150.
(31) Woo, H.-S.; Na, C. W.; Kim, I.-D.; Lee, J.-H. Highly sensitive and selective trimethylamine sensor using one-dimensional ZnO−Cr_2O_3hetero-nanostructures. *Nanotechnology* **2012**, *23*, No. 245501.
(32) Shouli, B.; Liangyuan, C.; Dianqing, L.; Wensheng, Y.; Pengcheng, Y.; Zhiyong, L.; Aifan, C.; Liu, C. C. Different morphologies of ZnO nanorods and their sensing property. *Sens. Actuators, B* **2010**, *146*, 129−137.
(33) Diéguez, A.; Romano-Rodríguez, A.; Morante, J. R.; Weimar, U.; Schweizer-Berberich, M.; Göpel, W. Morphological analysis of nanocrystalline SnO_2 for gas sensor applications. *Sens. Actuators, B* **1996**, *31*, 1−8.
(34) Park, S.; Hong, T.; Jung, J.; Lee, C. Room temperature hydrogen sensing of multiple networked ZnO/WO_3 core−shell nanowire sensors under UV illumination. *Curr. Appl. Phys.* **2014**, *14*, 1171−1175.
(35) Hsu, C.-L.; Jhang, B.-Y.; Kao, C.; Hsueh, T.-J. UV-illumination and Au-nanoparticles enhanced gas sensing of p-type Na-doped ZnO nanowires operating at room temperature. *Sens. Actuators, B* **2018**, *274*, 565−574.
(36) Wang, L.; Lou, Z.; Fei, T.; Zhang, T. Enhanced acetone sensing performances of hierarchical hollow Au-loaded NiO hybrid structures. *Sens. Actuators, B* **2012**, *161*, 178−183.
(37) Shingange, K.; Swart, H.; Mhlongo, G. H. Au functionalized ZnO rose-like hierarchical structures and their enhanced NO_2 sensing performance. *Phys. B* **2018**, *535*, 216−220.
(38) Cui, W.; Kang, X.; Zhang, X.; Zheng, Z.; Cui, X. Facile synthesis of porous cubic microstructure of Co_3O_4 from ZIF-67 pyrolysis and its Au doped structure for enhanced acetone gas-sensing. *Phys. E* **2019**, 165.
(39) Rong, Q.; Zhang, Y.; Hu, J.; Li, K.; Wang, H.; Chen, M.; Lv, T.; Zhu, Z.; Zhang, J.; Liu, Q. Design of ultrasensitive Ag-$LaFeO_3$ methanol gas sensor based on quasi molecular imprinting technology. *Sci. Rep.* **2018**, *8*, No. 14220.
(40) Chen, Q.; Wang, Y.; Wang, M.; Ma, S.; Wang, P.; Zhang, G.; Chen, W.; Jiao, H.; Liu, L.; Xu, X. Enhanced acetone sensor based on Au functionalized In-doped $ZnSnO_3$ nanofibers synthesized by electrospinning method. *J. Colloid Interface Sci.* **2019**, *543*, 285−299.
(41) Wang, L.; Fu, H.; Jin, Q.; Jin, H.; Haick, H.; Wang, S.; Yu, K.; Deng, S.; Wang, Y. Directly transforming SnS_2 nanosheets to hierarchical SnO_2 nanotubes: Towards sensitive and selective sensing of acetone at relatively low operating temperatures. *Sens. Actuators, B* **2019**, *292*, 148−155.
(42) Li, J.; Wang, L.; Liu, Z.; Wang, Y.; Wang, S. Au-modified α-Fe_2O_3 columnar superstructures assembled with nanoplates and their highly improved acetone sensing properties. *J. Alloys Compd.* **2017**, *728*, 944−951.
(43) Koo, W.-T.; Jang, J.-S.; Choi, S.-J.; Cho, H.-J.; Kim, I.-D. Metal−organic framework templated catalysts: dual sensitization of PdO−ZnO composite on hollow SnO_2 nanotubes for selective acetone sensors. *ACS Appl. Mater. Interfaces* **2017**, *9*, 18069−18077.
(44) Zhang, J.; Song, P.; Li, Z.; Zhang, S.; Yang, Z.; Wang, Q. Enhanced trimethylamine sensing performance of single-crystal MoO_3 nanobelts decorated with Au nanoparticles. *J. Alloys Compd.* **2016**, *685*, 1024−1033.

DOI: 10.1021/acsomega.9b01989
ACS Omega 2019, 4, 19018−19029

(45) Jin, C.; Kim, H.; Park, S.; Kim, H. W.; Lee, S.; Lee, C. Enhanced ethanol gas sensing properties of SnO_2 nanobelts functionalized with Au. *Ceram. Int.* **2012**, *38*, 6585−6590.
(46) Majhi, S. M.; Naik, G. K.; Lee, H.-J.; Song, H.-G.; Lee, C.-R.; Lee, I.-H.; Yu, Y.-T. Au@NiO core-shell nanoparticles as a p-type gas sensor: Novel synthesis, characterization, and their gas sensing properties with sensing mechanism. *Sens. Actuators, B* **2018**, *268*, 223−231.
(47) Ma, L.; Ma, S. Y.; Qiang, Z.; Xu, X. L.; Chen, Q.; Yang, H. M.; Chen, H.; Ge, Q.; Zeng, Q. Z.; Wang, B. Q. Preparation of Co-doped $LaFeO_3$ nanofibers with enhanced acetic acid sensing properties. *Mater. Lett.* **2017**, *200*, 47−50.
(48) Toàn, N. N.; Saukko, S.; Lantto, V. Gas sensing with semiconducting perovskite oxide $LaFeO_3$. *Phys. B* **2003**, *327*, 279−282.
(49) Wei, W.; Guo, S.; Chen, C.; Sun, L.; Chen, Y.; Guo, W.; Ruan, S. High sensitive and fast formaldehyde gas sensor based on Ag-doped $LaFeO_3$ nanofibers. *J. Alloys Compd.* **2017**, *695*, 1122−1127.
(50) Xiang, J.; Chen, X.; Zhang, X.; Gong, L.; Zhang, Y.; Zhang, K. Preparation and characterization of Ba-doped $LaFeO_3$ nanofibers by electrospinning and their ethanol sensing properties. *Mater. Chem. Phys.* **2018**, *213*, 122−129.
(51) Zhang, N.; Ruan, S.; Yin, Y.; Li, F.; Wen, S.; Chen, Y. Self-Sacrificial Template-Driven $LaFeO_3/\alpha$-Fe_2O_3 Porous Nano-Octahedrons for Acetone Sensing. *ACS Appl. Nano Mater.* **2018**, *1*, 4671−4681.
(52) Zhu, H.; Zhang, P.; Dai, S. Recent Advances of Lanthanum-Based Perovskite Oxides for Catalysis. *ACS Catal.* **2015**, *5*, 6370−6385.
(53) Chen, M.; Zhang, D.; Hu, J.; Wang, H.; Zhang, Y.; Li, K.; Rong, Q.; Zhou, S.; Zhang, J.; Zhu, Z.; Liu, Q. Excellent toluene gas sensing properties of molecular imprinted Ag-$LaFeO_3$ nanostructures synthesized by microwave-assisted process. *Mater. Res. Bull.* **2019**, *111*, 320−328.
(54) Zhang, Y.; Zhang, J.; Chen, J.; Zhu, Z.; Liu, Q. Improvement of response to formaldehyde at Ag−$LaFeO_3$ based gas sensors through incorporation of SWCNTs. *Sens. Actuators, B* **2014**, *195*, 509−514.
(55) Gu, F.; Wang, H.; Han, D.; Wang, Z. Enhancing the sensing performance of SnO_2 inverse opal thin films by In and Au doping. *Sens. Actuators, B* **2017**, *245*, 1023−1031.
(56) Korotcenkov, G.; Gulina, L.; Cho, B.; Han, S.; Tolstoy, V. SnO_2−Au nanocomposite synthesized by successive ionic layer deposition method: Characterization and application in gas sensors. *Mater. Chem. Phys.* **2011**, *128*, 433−441.
(57) Xia, X.; Dong, X.; Wei, Q.; Cai, Y.; Lu, K. Formation mechanism of porous hollow SnO_2 nanofibers prepared by one-step electrospinning. *eXPRESS Polym. Lett.* **2012**, *6*, 169.
(58) Horzum, N.; Taşçıoglu, D.; Okur, S.; Demir, M. M. Humidity sensing properties of ZnO-based fibers by electrospinning. *Talanta* **2011**, *85*, 1105−1111.
(59) Horzum, N.; Muñoz-Espí, R.; Glasser, G.; Demir, M. M.; Landfester, K.; Crespy, D. Hierarchically structured metal oxide/silica nanofibers by colloid electrospinning. *ACS Appl. Mater. Interfaces* **2012**, *4*, 6338−6345.
(60) Lin, X.; Xiong, L.; Qi, G.; Shi, S.; Huang, C.; Chen, X.; Chen, X. Using butanol fermentation wastewater for biobutanol production after removal of inhibitory compounds by micro/mesoporous hyper-cross-linked polymeric adsorbent. *ACS Sustainable Chem. Eng.* **2015**, *3*, 702−709.
(61) Clavier, G. M.; Pozzo, J. L.; Bouas-Laurent, H.; Liere, C.; Roux, C.; Sanchez, C. Organogelators for making porous sol−gel derived silica at two different length scales. *J. Mater. Chem.* **2000**, *10*, 1725−1730.
(62) Choi, K.-I.; Kim, H.-R.; Lee, J.-H. Enhanced CO sensing characteristics of hierarchical and hollow In_2O_3 microspheres. *Sens. Actuators, B* **2009**, *138*, 497−503.
(63) Zhang, X.-D.; Zhang, W.-L.; Cai, Z.-X.; Li, Y.-K.; Yamauchi, Y.; Guo, X. $LaFeO_3$ porous hollow micro-spindles for NO_2 sensing. *Ceram. Int.* **2019**, 5240.
(64) Dai, Z.; Lee, C.-S.; Kim, B.-Y.; Kwak, C.-H.; Yoon, J.-W.; Jeong, H.-M.; Lee, J.-H. Honeycomb-like periodic porous $LaFeO_3$ thin film chemiresistors with enhanced gas-sensing performances. *ACS Appl. Mater. Interfaces* **2014**, *6*, 16217−16226.
(65) Ikeo, N.; Iijima, Y.; Niimura, N.; Sigematsu, M.; Tazawa, T.; Matsumoto, S.; Kojima, K.; Nagasawa, Y. *Handbook of X-ray Photoelectron Spectroscopy*; JEOL UK: Welwyn Garden City, 1991.
(66) Thirumalairajan, S.; Girija, K.; Mastelaro, V. R.; Ponpandian, N. Surface morphology-dependent room-temperature $LaFeO_3$ nanostructure thin films as selective NO_2 gas sensor prepared by radio frequency magnetron sputtering. *ACS Appl. Mater. Interfaces* **2014**, *6*, 13917−13927.
(67) Wiranwetchayan, O.; Promnopas, S.; Phadungdhitidhada, S.; Phuruangrat, A.; Thongtem, T.; Singjai, P.; Thongtem, S. Characterization of perovskite $LaFeO_3$ synthesized by microwave plasma method for photocatalytic applications. *Ceram. Int.* **2019**, *45*, 4802−4809.
(68) Casaletto, M.; Longo, A.; Martorana, A.; Prestianni, A.; Venezia, A. XPS study of supported gold catalysts: the role of Au^0 and $Au^{+\delta}$ species as active sites. *Surf. Interface Anal.* **2006**, *38*, 215−218.
(69) Lee, W.-Y.; Yun, H. J.; Yoon, J.-W. Characterization and magnetic properties of $LaFeO_3$ nanofibers synthesized by electrospinning. *J. Alloys Compd.* **2014**, *583*, 320−324.
(70) Thirumalairajan, S.; Girija, K.; Hebalkar, N. Y.; Mangalaraj, D.; Viswanathan, C.; Ponpandian, N. Shape evolution of perovskite $LaFeO_3$ nanostructures: a systematic investigation of growth mechanism, properties and morphology dependent photocatalytic activities. *RSC Adv.* **2013**, *3*, 7549−7561.
(71) Stoerzinger, K. A.; Comes, R.; Spurgeon, S. R.; Thevuthasan, S.; Ihm, K.; Crumlin, E. J.; Chambers, S. A. Influence of $LaFeO_3$ surface termination on water reactivity. *J. Phys. Chem. Lett.* **2017**, *8*, 1038−1043.
(72) Wang, C.; Yin, L.; Zhang, L.; Xiang, D.; Gao, R. Metal oxide gas sensors: sensitivity and influencing factors. *Sensors* **2010**, *10*, 2088−2106.
(73) Zhang, S.; Song, P.; Zhang, J.; Yan, H.; Li, J.; Yang, Z.; Wang, Q. Highly sensitive detection of acetone using mesoporous In_2O_3 nanospheres decorated with Au nanoparticles. *Sens. Actuators, B* **2017**, *242*, 983−993.
(74) Shingange, K.; Tshabalala, Z.; Ntwaeaborwa, O.; Motaung, D.; Mhlongo, G. Highly selective NH_3 gas sensor based on Au loaded ZnO nanostructures prepared using microwave-assisted method. *J. Colloid Interface Sci.* **2016**, *479*, 127−138.
(75) Kim, H.-J.; Jeong, H.-M.; Kim, T.-H.; Chung, J.-H.; Kang, Y. C.; Lee, J.-H. Enhanced ethanol sensing characteristics of In_2O_3-decorated NiO hollow nanostructures via modulation of hole accumulation layers. *ACS Appl. Mater. Interfaces* **2014**, *6*, 18197−18204.
(76) Cao, J.; Wang, S.; Zhang, H.; Zhang, T. Facile construction of Co_3O_4 porous microspheres with enhanced acetone gas sensing performances. *Mater. Sci. Semicond. Process.* **2019**, *101*, 10−15.
(77) Qu, F.; Thomas, T.; Zhang, B.; Zhou, X.; Zhang, S.; Ruan, S.; Yang, M. Self-sacrificing templated formation of $Co_3O_4/ZnCo_2O_4$ composite hollow nanostructures for highly sensitive detecting acetone vapor. *Sens. Actuators, B* **2018**, *273*, 1202−1210.
(78) Mhlongo, G.; Motaung, D.; Cummings, F.; Swart, H.; Ray, S. A highly responsive NH_3 sensor based on Pd-loaded ZnO nanoparticles prepared via a chemical precipitation approach. *Sci. Rep.* **2019**, *9*, No. 9881.
(79) Malik, R.; Tomer, V. K.; Kienle, L.; Chaudhary, V.; Nehra, S.; Duhan, S. Ordered mesoporous Ag−ZnO@ CN nanohybrid as highly efficient bifunctional sensing material. *Adv. Mater. Interfaces* **2018**, *5*, No. 1701357.
(80) Wang, T.; Can, I.; Zhang, S.; He, J.; Sun, P.; Liu, F.; Lu, G. Self-assembly template driven 3D inverse opal microspheres functionalized with catalyst nanoparticles enabling a highly efficient chemical sensing platform. *ACS Appl. Mater. Interfaces* **2018**, *10*, 5835−5844.

DOI: 10.1021/acsomega.9b01989
ACS Omega 2019, 4, 19018−19029

(81) Wang, C.; Rong, Q.; Zhang, Y.; Hu, J.; Zi, B.; Zhu, Z.; Zhang, J.; Liu, Q. Molecular imprinting Ag-$LaFeO_3$ spheres for highly sensitive acetone gas detection. *Mater. Res. Bull.* **2019**, *109*, 265−272.
(82) Rai, P.; Khan, R.; Raj, S.; Majhi, S. M.; Park, K.-K.; Yu, Y.-T.; Lee, I.-H.; Sekhar, P. K. Au@Cu_2O core−shell nanoparticles as chemiresistors for gas sensor applications: effect of potential barrier modulation on the sensing performance. *Nanoscale* **2014**, *6*, 581−588.
(83) Ma, Q.; Fang, Y.; Liu, Y.; Song, J.; Fu, X.; Li, H.; Chu, S.; Chen, Y. Facile synthesis of ZnO morphological evolution with tunable growth habits: Achieving superior gas-sensing properties of hemispherical ZnO/Au heterostructures for triethylamine. *Phys. E* **2019**, *106*, 180−186.
(84) Murade, P.; Sangawar, V.; Chaudhari, G.; Kapse, V.; Bajpeyee, A. Acetone gas-sensing performance of Sr-doped nanostructured $LaFeO_3$ semiconductor prepared by citrate sol−gel route. *Curr. Appl. Phys.* **2011**, *11*, 451−456.
(85) Wang, X.; Qin, H.; Pei, J.; Chen, Y.; Li, L.; Xie, J.; Hu, J. Sensing performances to low concentration acetone for palladium doped $LaFeO_3$ sensors. *J. Rare Earths* **2016**, *34*, 704−710.
(86) Chen, Y.; Qin, H.; Wang, X.; Li, L.; Hu, J. Acetone sensing properties and mechanism of nano-$LaFeO_3$ thick-films. *Sens. Actuators, B* **2016**, *235*, 56−66.
(87) Zhang, L.; Qin, H.; Song, P.; Hu, J.; Jiang, M. Electric properties and acetone-sensing characteristics of $La_{1-x}Pb_xFeO_3$ perovskite system. *Mater. Chem. Phys.* **2006**, *98*, 358−362.
(88) Liu, X.; Ji, H.; Gu, Y.; Xu, M. Preparation and acetone sensitive characteristics of nano-$LaFeO_3$ semiconductor thin films by polymerization complex method. *Mater. Sci. Eng., B* **2006**, *133*, 98−101.
(89) Song, P.; Zhang, H.; Han, D.; Li, J.; Yang, Z.; Wang, Q. Preparation of biomorphic porous $LaFeO_3$ by sorghum straw biotemplate method and its acetone sensing properties. *Sens. Actuators, B* **2014**, *196*, 140−146.

DOI: 10.1021/acsomega.9b01989
ACS Omega 2019, 4, 19018−19029